Materials Science & Engineering A 867 (2023) 144727

Contents lists available at ScienceDirect

Materials Science & Engineering A

journal homepage: www.elsevier.com/locate/msea

Excellent dynamic-mechanical behavior assisted by stacking faults in a nano-coherent high-entropy alloy

J.L. Yuan [a], Z.M. Jiao [b], Z. Wang [b], J.W. Qiao [a,c,*], P.D. Han [a], Z.H. Wang [b,**], P.K. Liaw [d]

[a] College of Materials Science and Engineering, Taiyuan University of Technology, Taiyuan, 030024, China
[b] Institute of Applied Mechanics, College of Mechanical and Vehicle Engineering, Taiyuan University of Technology, Taiyuan, 030024, China
[c] Key Laboratory of Interface Science and Engineering in Advanced Materials, Ministry of Education, Taiyuan University of Technology, Taiyuan, 030024, China
[d] Department of Materials Science and Engineering, The University of Tennessee, Knoxville, TN, 37996-2200, USA

ARTICLE INFO

Keywords:
High-entropy alloy
Precipitation strengthening
Dynamic tension
Deformation mechanisms
Stacking faults

ABSTRACT

In the current work, the coherent $L1_2$-phases-strengthened $Co_{40}Cr_{20}Ni_{30}Mo_2Al_4Ti_4$ (in atomic percent, at.%) high-entropy alloy (HEA) exhibits an excellent strength-plasticity synergy during dynamic tension. The diameter and volume fraction of $L1_2$ precipitates are about 7.8 nm and 9.85%, respectively. When the strain rate is 1700/s, the yield strength of the alloy is 950 MPa, the ultimate tensile strength is up to 1725 MPa, and the elongation remains at 40%. The plastic deformation of the alloy in a quasi-static state is dominated by dislocations. During dynamic tension, stacking faults contribute to the high strength and effective work hardening of the alloy as an additional deformation mechanism. The present work provides a basic theoretical guidance for understanding the dynamic-deformation behaviors and mechanisms of precipitation-strengthened HEAs.

1. Introduction

In recent years, high-entropy alloys (HEAs) have attracted extensive attention and related research contents have proliferated due to their multi-component design concept and the resulting excellent mechanical properties [1–5]. Among them, a large number of reports on precipitation strengthening have proved that it is a powerful means to strengthen face-centered-cubic (fcc) HEAs, especially the precipitation of coherent ordered $L1_2$ phases [6,7]. In addition, the explorations of such alloys are not limited to the mechanical properties at room temperature, but also involve some extreme service environments, such as ultra-low temperatures in liquid-nitrogen and even liquid-helium conditions and high temperatures above 900 °C [8–10]. Fortunately, under these service conditions, these precipitation-strengthened HEAs have shown great potential as structural application materials.

The strain rate is another key factor affecting the mechanical response of materials except temperature. Compared with traditional fcc pure metals and alloys, fcc HEAs show stronger dependence on temperature and strain rate [11]. However, these studies on temperature-strain rate-dependent mechanical properties are all based on the strain-rate jump tests in the quasi-static loading range [12–15]. In order to fully tap the application potential of HEAs, it is essential to further investigate and explore their mechanical behaviors and deformation mechanisms under high strain rates to meet the requirements of the aviation industry, automotive engineering, earthquake and other fields [16–18]. In contrast to quasi-static deformation, the alloys are prone to produce adiabatic shear bands and deformation twins during dynamic deformation [19,20]. The research on dynamic-compression deformation of the CoCrFeMnNi HEA shows that it is easier to reach the critical twinning stress under dynamic conditions, and twins are formed under smaller strains (the onset true plastic strain for twinning were determined to be 20.5% at strain rate of 10^{-4} s^{-1} and 6.2% at strain rate of 4700 s^{-1}), which leads to stronger work-hardening ability [19]. Similarly, the $Al_xCoCrFeNi$ (x = 0.1 and 0.3) alloy system also achieves strength doubling at high strain rates [21,22]. Moreover, the strain-rate sensitivity related to the microstructures of the alloys in this system has also been discussed [23–25]. However, the investigations on these alloys are mainly subjected to dynamic compressive or shear loading, and little is known about the mechanical behaviors under dynamic tension. CoCrNi medium-entropy alloy (MEA) and CoCrFeNi HEA have been shown to exhibit more significant strength-plasticity synergy in dynamic tension than in quasi-static deformation [26,27]. Unfortunately, most of the HEA systems used for dynamic-deformation research are single-phase solid solutions. At present, the studies on mechanical

* Corresponding author. College of Materials Science and Engineering, Taiyuan University of Technology, Taiyuan, 030024, China.
** Corresponding author.
E-mail addresses: qiaojunwei@gmail.com (J.W. Qiao), wangzh@tyut.edu.cn (Z.H. Wang).

https://doi.org/10.1016/j.msea.2023.144727
Received 4 January 2023; Received in revised form 27 January 2023; Accepted 30 January 2023
Available online 1 February 2023

responses and deformation mechanisms of precipitation-strengthened HEAs under dynamic tension have not been involved.

In the current work, the mechanical properties of the $Co_{40}Cr_{20}Ni_{30}Mo_2Al_4Ti_4$ (in atomic percent, at.%) HEA strengthened by coherent $L1_2$ phases under quasi-static and dynamic tension were evaluated, and the transformation of the strain-rate-related deformation mechanism was revealed. The present work provides a basic theoretical guidance for understanding the dynamic-deformation behaviors and mechanisms of precipitation-strengthened HEAs.

2. Materials and methods

The ingots with the nominal composition of $Co_{40}Cr_{20}Ni_{30}Mo_2Al_4Ti_4$ (in atomic percent, at.%) were obtained by vacuum-arc melting under a Ti-gettered argon atmosphere. Each ingot was flipped and re-melted more than five times to ensure the chemical uniformity. Then, the 50 × 20 × 5 mm^3 (length × width × thickness) thin plates were prepared by a water-cooled copper-mold suction-casting method. The as-cast plates were first homogenized at 1200 °C for 2 h. Then, cold rolling was carried out with a total reduction ratio of 80% (the thickness changed from 5 to 1 mm). Subsequently, annealing at 1200 °C for 3 min to achieve fully recrystallized microstructures. Finally, aged at 800 °C for 1 h. All heat treatments were conducted in the air and followed by water quenching.

Dog-bone-shaped specimens with gauge dimensions of 12.5 × 3 × 1 mm^3 and 10 × 3 × 1 mm^3 were fabricated by electro-discharge machining for quasi-static and dynamic tensile tests, respectively. Quasi-static tensile tests were performed on an Instron 5969 universal testing machine, and dynamic tensile tests were carried out, using a split Hopkinson tensile-bar (SHTB) apparatus. At least three samples were measured in each case to ensure the reliability of the data.

The phase identification was conducted, using X-ray diffraction (XRD) with Cu-Ka radiation. The scanning angle range of 2θ is 20°–80°. The microstructures of the alloy were characterized by scanning electron microscopy (SEM, Phenom XL), electron backscatter diffraction (EBSD) (the scanning step is 1 μm), and transmission electron microscopy (TEM, FEI Tecnai F30) with the selected area electron diffraction (SAED). For SEM and EBSD analyses, the surfaces of the samples were ground to 2000 grit SiC paper, and then electrochemically polished with a $HClO_4$:C_2H_6O = 1:9 solution (in a volume percent, vol%) with a direct-current (DC) voltage of 20 V at 298 K. For TEM analyses, the samples were firstly mechanically ground to a thickness below 30 μm and then punched into 3 mm-diameter discs. Finally, twin-jet electro-polishing was performed, employing the same electrolyte at a voltage of 20 V and a temperature of about - 10 °C.

3. Results

3.1. Initial microstructures

Fig. 1 exhibits the microstructural characterization of the current alloy. The aged samples are uniform equiaxed grains and contain quantities of annealing twins, as shown in the SEM image of Fig. 1(a). Excluding twin boundaries, the average grain size of the current alloy is about 86.3 μm by a linear intercept method. The inverse pole figure (IPF) map of Fig. 1(b) displays the basically random grain orientation. The average grain size, including twin boundaries determined by EBSD, is about 33.6 μm, as shown in the statistical graph of the grain-size distribution in Fig. 1(e). Fig. 1(c) is the texture IPF map constructed for the crystallographic orientation along the rolling direction, indicating weak <001> and <111> silk textures in the alloy, which are often observed in fcc alloys annealed after cold rolling. Only one set of fcc diffraction peaks can be identified in the XRD pattern [Fig. 1(d)], but the subsequent results show that the alloy is fcc + $L1_2$ dual-phase structure. Fig. 1(f) shows the misorientation angle distribution of grains, where the number fraction of grains with a misorientation angle of 60° is as high as 0.6, which means a high proportion of Σ3 annealing-twin boundaries. The illustration is an enlarged view of the local area in Fig. 1(b), where the white arrows indicate some annealing twins.

The microstructures of the alloy were further revealed by the TEM analysis, as presented in Fig. 2. Fig. 2(a) is the dark-field (DF) TEM image of the alloy, in which fine and dispersed spherical particles are uniformly distributed in the matrix. Fig. 2(b) shows the SAED pattern

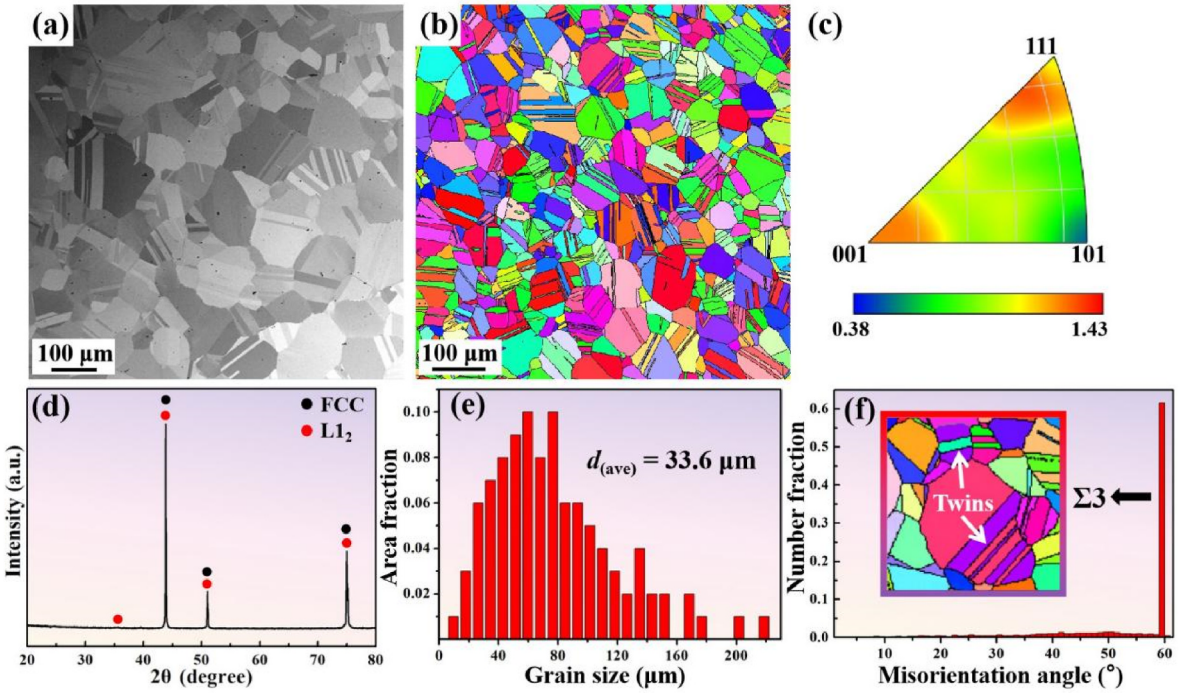

Fig. 1. The initial microstructures of the current alloy. (a) SEM image; (b) Inverse pole figure map; (c) Texture inverse pole figure map; (d) XRD pattern; The distribution of (e) grain size and (f) grain misorientation angles corresponding to the area of (b). The inset shows an enlarged view of some twin boundaries (indicated by white arrows).

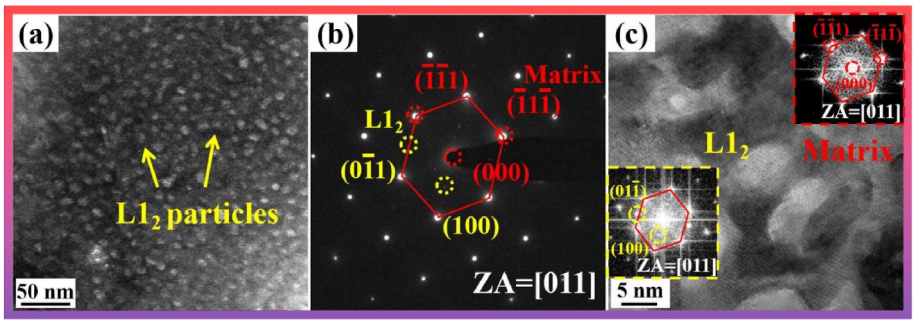

Fig. 2. TEM observations of the microstructures. (a) Dark-field TEM image shows the uniform dispersion distribution of $L1_2$ particles; (b) A SAED pattern along the [011] zone axis showing the $L1_2$ structure; (c) High-resolution TEM image. The insets are the fast Fourier transform images of the matrix and $L1_2$ phases.

obtained along the [011] zone axis, which is consistent with the previous XRD results, confirming that these spherical particles are ordered $L1_2$ phases. Through statistics on several DF-TEM images, it is determined that the diameter of $L1_2$ particles is about 7.8 nm, and the volume fraction is approximately 9.85%. Fig. 2(c) is a high-resolution TEM (HRTEM) image of the alloy, which proves the completely coherent interface relationship between the matrix and the precipitates. Furthermore, the illustrations in the red and yellow rectangular boxes are the fast Fourier transform (FFT) images of the matrix and the precipitate, respectively. The matrix is indexed to be fcc, and the precipitates have additional (001) and (011) superlattice diffraction spots, which further authenticates the $L1_2$ phase structure of the precipitates.

3.2. Quasi-static and dynamic mechanical properties

Quasi-static and dynamic tensile tests were conducted to further evaluate the performance potential of this alloy, as shown in Fig. 3. The engineering stress-strain curves of the alloy under quasi-static (10^{-3}/s, 10^{-2}/s, and 10^{-1}/s) and dynamic (1100/s and 1700/s) tension are shown in Fig. 3(a). In the quasi-static loading range, the yield strength increases slightly with the increase of strain rate, from 680 MPa at 10^{-3}/s to 745 MPa at 10^{-1}/s. In contrast, the ultimate tensile strength remains stable while the elongation decreases from 46.5% to 36.5%, as the strain rate increases. It should be noted that the tensile curve with a strain rate of 1100/s is not completely recorded because the samples are not broken. Therefore, the table in Fig. 3(a) does not show the ultimate tensile strength and elongation under this condition, and only the yield strength of 820 MPa is obtained. Compared with the strain rate of 10^{-3}/s, when the strain rate increases to 1700/s, the yield and ultimate tensile strengths increase by 40% and 59%, respectively, reaching 950 MPa and 1725 MPa. However, unlike the effect of strain rate on plasticity in the quasi-static range, this alloy has no obvious embrittlement during dynamic tension, and still maintains a large elongation of 40%. Fig. 3(b) exhibits the curves of the strain-hardening rate, θ,/true stress versus true strain under quasi-static and dynamic tension. According to their characteristics, the work-hardening behavior can be divided into three stages. In the first stage I, namely the elastic-plastic transition zone, the work-hardening rates drop sharply. In the second stage II, the work-hardening rates increase slowly in quasi-static states and decrease in dynamic states. In the third stage III, the work-hardening rates of both of them decrease rapidly. The work-hardening ability under quasi-static and dynamic tension shows great difference in the stage II, which is closely related to their potential characteristic micro-deformation mechanisms. This feature will be discussed in the next chapter.

Fig. 4 summarizes the mechanical properties of the current alloy, Al alloys, Mg alloys, Ti alloys, TRIP/TWIP steels, fcc HEAs, and other metals in dynamic tension/compression (see supplementary materials for data points in the figures) [27]. The strain rates are all in the order of 1000. The yield strength of traditional Al and Mg alloys is low, usually about 100–500 MPa, and the elongation is within 40%. TRIP/TWIP steels, austenitic steels, and some fcc HEAs possess medium strength-plastic combination with yield strengths of about 400–700 MPa and elongations of 30%–60%. Dual-phase steels have ultra-high strengths, up to about 1500 MPa. However, the plastic loss is great, and the elongation is less than 10%. In contrast, the current alloy shows an excellent strength-plasticity synergy.

3.3. Quasi-static deformation microstructures

Fig. 5 presents the EBSD results of the microstructures near the fracture of the sample with a strain rate of 10^{-3}/s. After large plastic deformation, the grains are significantly elongated along the tensile direction, and substantial slip lines are formed in the grains, as shown in the band-contrast map in Fig. 5(a). The orientation of grains in deformed samples is no longer random, and the typical strong <111> texture in fcc alloys is found along the tensile direction, as presented in Fig. 5(b) and (d). Fig. 5(c) shows the distribution of geometrically necessary dislocations of the sample, suggesting relatively uniform plastic

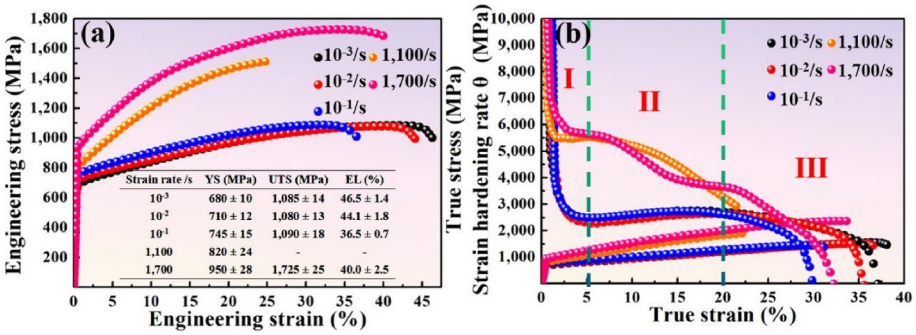

Fig. 3. Mechanical properties of the alloy. (a) Engineering stress-strain curves under quasi-static and dynamic tension; (b) Strain-hardening rate, θ,/true stress versus true strain.

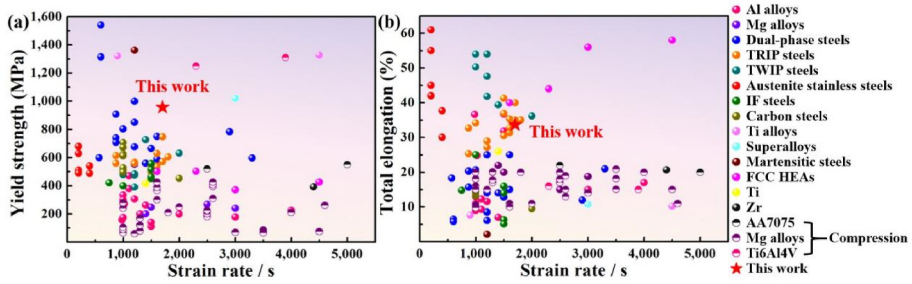

Fig. 4. Comparison of dynamic-mechanical properties among the current alloy and other metals and alloys. The maps of (a) yield strength versus strain rate and (b) total elongation versus strain rate (the yield strength and corresponding total elongation are obtained from the true stress-strain curves).

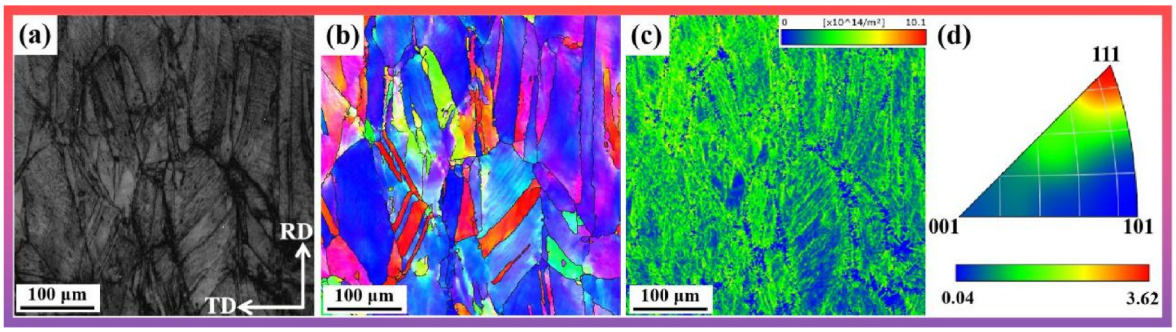

Fig. 5. EBSD characterizations of the sample with a strain rate of 10^{-3}/s. (a) Band-contrast map; (b) Inverse pole figure map; (c) Geometrically necessary dislocations; (d) Texture inverse pole figure map.

deformation. In order to unveil the micro-deformation mechanisms of the current alloy, it was characterized by TEM, as shown in Fig. 6. The plastic deformation in a quasi-static state is dominated by dislocations, and it displays obvious planar-slip characteristics, that is, dislocation arrays along two directions. The planar-slip bands from different slip systems intersect each other, forming a Taylor lattice structure with a spacing of several hundred nanometers. These network structures, which are refined with deformation, also subdivide grains, shorten the average free path of dislocation movement, and cause continuous work hardening of materials. Fig. 6(b) indicates the slip traces of dislocations.

3.4. Dynamic deformation microstructures

Fig. 7(a) and (f) present samples with strain rates of 1100/s and 1700/s, respectively. The actual elongation of the sample with a strain rate of 1100/s is 30%, which is still in the stage of uniform deformation, without necking, while the sample with a strain rate of 1700/s has a slight necking. Fig. 7(b–e) and (g-j) are the EBSD characterizations of the red and yellow rectangular areas in Fig. 7(f), respectively, that is, the microstructures far away from and near the fracture surface. The local strain distribution in different regions is also uneven. There is no obvious deformation of grains in the area far from the fracture, and the grains show a slightly weak <111> texture along the tensile direction. As shown in Fig. 7(d), a small amount of dislocations are detected in this region, indicating limited plastic deformation. The higher dislocation density near the grain boundaries reveals that dislocation slip is blocked at the interfaces, and plastic deformation preferentially occurs at the grain boundaries. The grains near the fracture surface are mildly elongated and the dislocation slip and multiplication are further increased. As shown in Fig. 7(i), severe dislocation accumulation and entanglement are found in this area, and dislocation density is significantly increased, which means that higher plastic deformation is sustained near the fracture. Moreover, the sample presents a stronger <111> texture than the quasi-static one.

The two samples after dynamic tension were characterized by TEM to clarify their micro-deformation mechanisms under dynamic conditions, as exhibited in Fig. 8. Compared to the quasi-static deformation, the planar slip feature disappears in the sample with a strain rate of 1100/s, and is replaced by extensive dislocation entanglement [Fig. 8 (a)]. Furthermore, additional nanoscale stacking faults appear in the

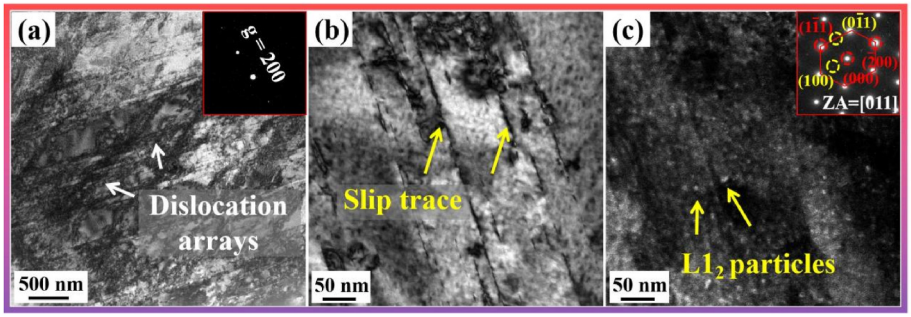

Fig. 6. TEM images of the quasi-static deformed sample. (a) Bright-field TEM image showing the planar-slip characteristics of dislocations; (b) Slip traces of dislocations; (c) Dark-field TEM image of $L1_2$ phases.

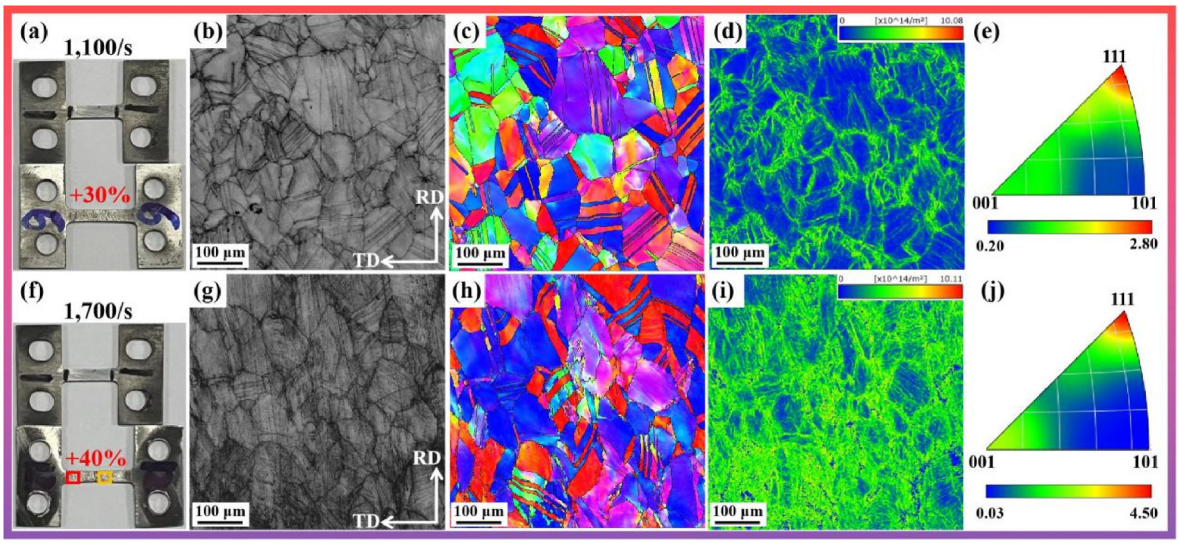

Fig. 7. Dynamic tensile samples and EBSD characterization. Physical pictures of samples with strain rates of (a) 1100/s and (f) 1700/s, compared with unstretched samples; EBSD images of the area (b–e) far away from and (g–j) near the fracture surface of the sample with a strain rate of 1700/s; (b, g) Band-contrast map; (c, h) Inverse pole figure map; (d, i) Geometrically necessary dislocations; (e, j) Texture inverse pole figure map.

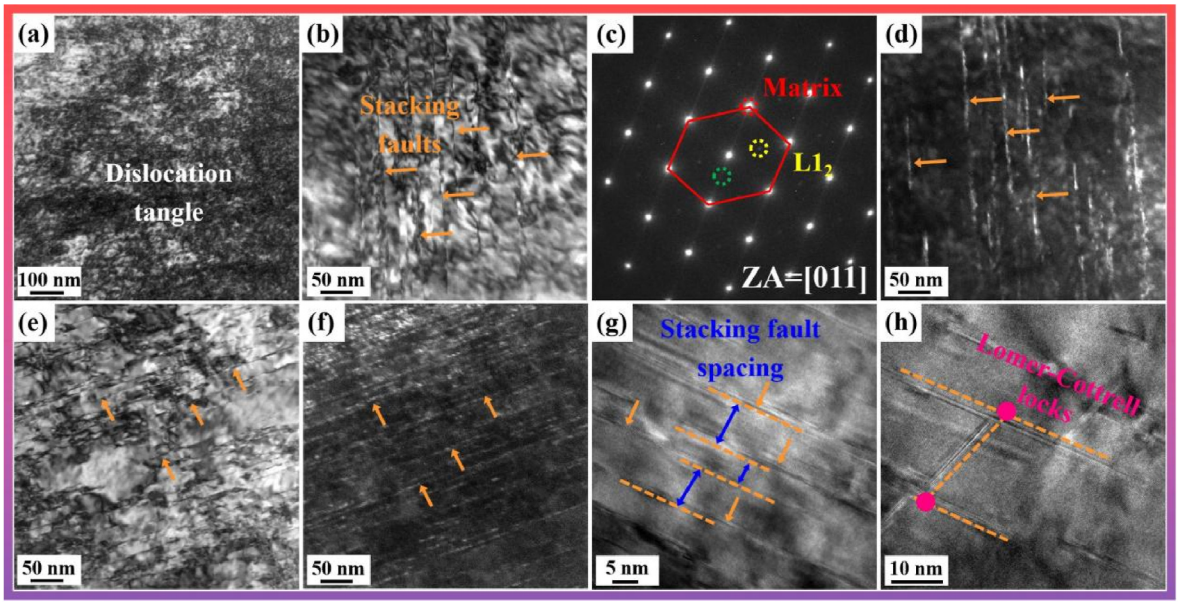

Fig. 8. TEM images of samples with strain rates of (a–d) 1100/s and (e–h) 1700/s. Bright-field TEM image of (a) dislocations and (b) stacking faults; (c) A SAED pattern showing the $L1_2$ structure and stacking faults; (d) Dark-field TEM image of stacking faults; (e) Bright-field and corresponding (f) dark-field TEM images of stacking faults; (g) High-resolution TEM image of stacking faults; (h) Lomer-Cottrell locks.

microstructures, and the corresponding SAED pattern displays "awn lines" symbolizing stacking faults, as exhibited in the green circle of Fig. 8(c). The DF-TEM analysis is performed on the green circle area to testify stacking faults more intuitively. As shown in Fig. 8(d), the bright parts are stacking faults, and the spacing between adjacent stacking faults is about 17 nm. The sample with a strain rate of 1700/s has a large deformation, and the density of stacking faults increases substantially. At this time, the spacing of stacking faults is refined to about 8 nm, as shown in Fig. 8(e–g). Besides, the interaction of stacking faults on different slip planes forms Lomer-Cottrell (L-C) locks, which act as dislocation sources and powerful obstacles to pinning dislocations, facilitating the effective strain hardening of the alloy [Fig. 8(h)] [28,29].

3.5. Fracture morphologies

Fig. 9 presents the low- and high magnification fracture morphologies of this alloy at the strain rates of 10^{-3}/s, 10^{-2}/s, 10^{-1}/s, and 1700/s, respectively. When the strain rate is 10^{-3}/s, the fracture surface is flat with relatively uniform dimples. When the strain rate increases to 10^{-2}/s, the roughness of the fracture surface increases significantly. The sheets formed by the connection of voids appear in local areas, and the dimples become less and shallower. When the strain rate continues to increase to 10^{-1}/s, the number of dimples decreases markedly, and intergranular cracks become more. Hence, in the quasi-static range, with the increase of the strain rate, the fracture mechanisms gradually transit from a ductile to brittle fracture, resulting in a continuous decline in the plasticity of the alloy. It is gratifying that the fracture morphology at the strain rate of 1700/s is similar to that at the strain rate of 10^{-3}/s, with

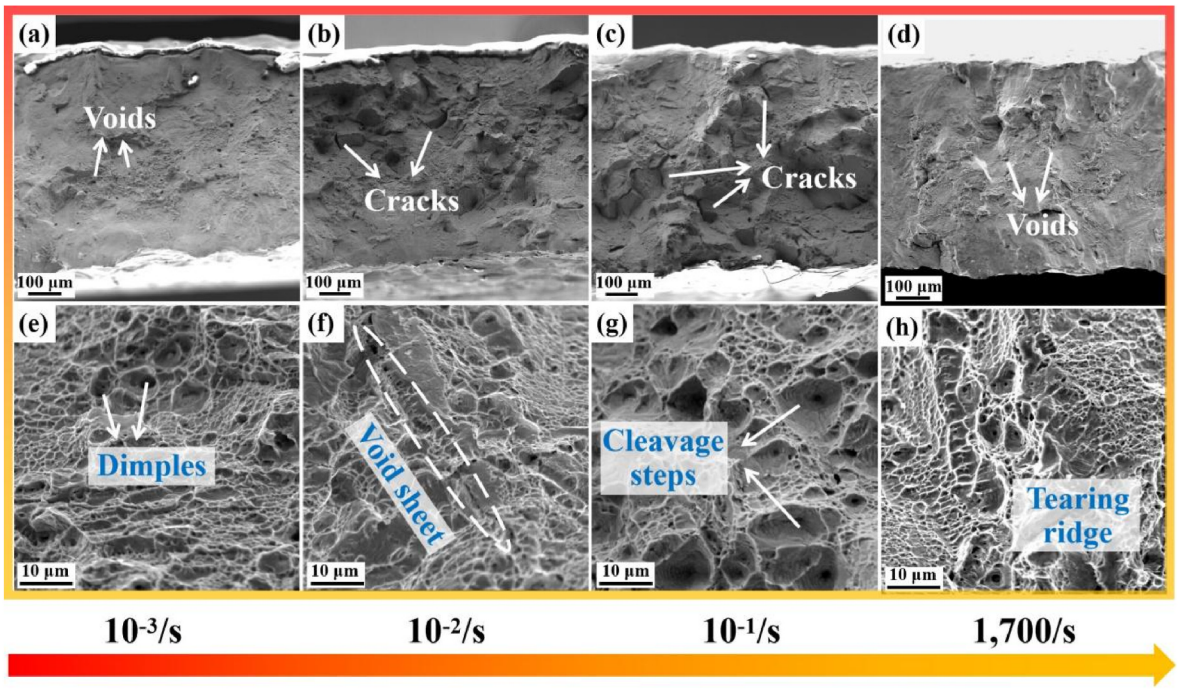

Fig. 9. Fracture morphologies of the samples tested at (a, e) 10^{-3}/s; (b, f) 10^{-2}/s; (c, g) 10^{-1}/s; and (d, h) 1700/s. (a–d) and (e–h) are the low- and high-magnification morphologies of the tensile fracture, respectively.

obvious dimples and tearing ridges. Consequently, the elongation of the alloy at a strain rate of 1700/s is equivalent to that at 10^{-3}/s.

4. Discussion

4.1. Precipitation strengthening

The coherent ordered $L1_2$ precipitates provide the high strength of the current alloy. In principle, when the precipitates are small in size and coherent with the matrix, the shear mechanism dominates the precipitation strengthening. Otherwise, the Orowan bypass mechanism plays a dominant role. The critical size of precipitates here is about 100 nm [30]. For a shear mechanism, coherent strengthening ($\Delta\sigma_{cs}$), modulus strengthening ($\Delta\sigma_{ms}$), and ordered strengthening ($\Delta\sigma_{os}$) are the main sources [31]. The larger value between the sum of the former two and the latter represents the contribution of precipitation strengthening. In view of the size of precipitates in this alloy is small enough, and the direct evidence of the coherence between the matrix and the precipitates shown in Fig. 2(c), it is reasonable and very reliable to select the shear mechanism for the quantitative calculation of precipitation strengthening. $\Delta\sigma_{cs}$, $\Delta\sigma_{ms}$, and $\Delta\sigma_{os}$ can be calculated by the following formulas [31]:

$$\Delta\sigma_{CS} = M\cdot\alpha_{\varepsilon}(G\cdot\varepsilon_c)^{\frac{3}{2}}\left(\frac{rf}{0.5Gb}\right)^{\frac{1}{2}} \quad (1)$$

$$\Delta\sigma_{MS} = 0.0055M(\Delta G)^{\frac{3}{2}}\left(\frac{2f}{G}\right)^{\frac{1}{2}}\left(\frac{r}{b}\right)^{\frac{3m}{2}-1} \quad (2)$$

$$\Delta\sigma_{OS} = 0.81M\frac{\gamma_{APB}}{2b}\left(\frac{3\pi f}{8}\right)^{\frac{1}{2}} \quad (3)$$

where $M = 3.06$ is the Taylor factor [32], α_{ε} and m are constants, equal to 2.6 and 0.85, respectively, $\varepsilon_c = 0.002$ is the constrained lattice-mismatch strain, G is the shear modulus of the matrix, r and f are the average radius and volume fraction of the precipitates, respectively, $b = 0.253$ nm is the Burger vector, ΔG is the difference between the shear modulus of the matrix and the precipitates (the shear moduli of the matrix and the precipitates are 88.7 GPa and 77.4 GPa, respectively [33, 34]), and $\gamma_{APB} = 200$ mJ/m^2 is the anti-phase boundary energy of the precipitates [35]. It is calculated that $\Delta\sigma_{cs}$, $\Delta\sigma_{ms}$, and $\Delta\sigma_{os}$ are 110 MPa, 64 MPa, and 334 MPa, respectively. So, the contribution of precipitation strengthening is 334 MPa, which accounts for one half of the yield strength of this alloy, indicating that coherent $L1_2$ phases have a remarkable strengthening effect on the matrix.

4.2. Excellent dynamic-mechanical properties

As shown in Figs. 3 and 4, the alloy possesses eminent dynamic-mechanical properties and strong work-hardening ability, which is originated from the synergistic effect of various plastic-deformation mechanisms, including the dislocation slip, stacking fault, and L-C locks.

The molecular dynamics simulation results of tensile deformation of $Al_{10}(CrCoFeNi)_{90}$ HEA shows that the introduction of nanotwins can improve the strength of the samples with equiaxed grains [36]. In addition, the strength of the alloy increases monotonously with the decrease of the twin boundary spacing [36]. In the same way, nano-scale deformation twins exhibit a prominent contribution to work hardening in plastic deformed high manganese steel [37]. This is similar to the stacking faults in the current alloy. Compared with quasi-static tension, the alloy possess higher strength under dynamic tension. When the strain rate increased from 1100/s to 1700/s, the spacing between adjacent stacking faults decreased, the stacking fault networks are refined, and the strength is accordingly improved. Similar to the twinning-induced plastic effect, the stacking fault networks are continuously formed and refined during the dynamic deformation process, effectively dividing the grains into smaller dislocation-motion regions. These nano-spaced stacked fault networks reduce the average free path of dislocation movement, resulting in a dynamic Hall-Patch effect [9, 38]. The stacking faults can not only hinder the movement of dislocations, but also serve as the favourable locations for producing partial dislocations. As a consequence, they can adapt to the plastic deformation in the lattice and maintain the ductility of the alloy. Additionally, co-planar stacking faults intersected with each other promote the

formation of stacking-fault networks and abundant sessile L-C locks. This L-C lock involves stacking fault band on two intersecting slip planes, so it can neither slide on two intersecting slip planes nor on its own slip plane. Therefore, they can pin the stacking fault networks to make them more stable. In general, these L-C locks, stacking faults and precipitates, as strong obstacles to dislocation movement and Frank-Read dislocation sources, stimulate the proliferation and accumulation of dislocations, and together contribute to the high strength and work hardening of the alloy [28,29]. During quasi-static deformation, dislocation motion is controlled by the thermal activation [24]. By comparison, the thermal-activation efficiency decreases during dynamic deformation. Besides, fast moving dislocations cause phonon scattering and increase the viscosity of dislocation motion [39,40]. Therefore, the phonon-drag effect in dynamic states and additional plastic-deformation mechanisms make the alloy possess both the high strength and large ductility in dynamic tension.

4.3. Dynamic-deformation mechanisms

Extensive deformation twins were detected in the microstructures of the quasi-static and dynamic tensile deformation of the single-phase CoCrNi MEA, and the density of deformation twins under dynamic tension has increased compared with that under quasi-static deformation [26]. Plastic deformation dominated by dislocation slip and deformation twins is also recognized in CoCrFeNi HEA under shock compression. The deformation twins under low velocity impacts appear as individual twins, while the deformation twins expand into twin bundles under high velocity impacts [41]. Unlike these cases, the current alloy does not form deformation twins during dynamic deformation. Based on the classical dislocation theory, the critical twinning stress, τ_{critical}, can be calculated by the following formula [42]:

$$\tau_{critical} = \frac{2\alpha G b_p}{D} + \frac{\gamma_{sf}}{b_p} + \tau_{fr} \tag{4}$$

where $\alpha = 0.5$ is a constant reflecting the characteristics of dislocation, $b_p = 0.147$ nm is the Burgers vector of the Shockley partial dislocation, D is the effective length of twinning sources, γ_{sf} is the stacking-fault energy, and τ_{fr} is the lattice-friction stress. $D = 15$ nm can be evaluated by $\sqrt{\frac{8}{3\pi f}}d - d$, where d is the diameter of precipitates [35]. It is clear that the first term in Formula 4 strongly depends on the source size, D. The nanoscale $L1_2$ phases in this alloy reduce the matrix channel to only 15 nm. Hence, the first term in Formula 4 is 870 MPa. Accordingly, the critical twinning normal stress is 2660 MPa. The contribution of the second term caused by the stacking-fault energy is 1097 MPa. The lattice friction stress of the third item is 218 MPa [43]. When the strain rate is 1700/s, the maximum true stress of the alloy in the tensile process is 2358 MPa, which is far less than the theoretical critical twinning stress (3975 MPa). Therefore, the formation of twins is suppressed. According to the above analysis, it can be concluded that fine and dispersed precipitates are not conducive to the formation of twins.

Specific details about the calculation of the stacking-fault energy are described as follows [44]:

$$\gamma_{sf} = 2\rho\Delta G^{\gamma\to\varepsilon} + 2\sigma^{\gamma\to\varepsilon} \tag{5}$$

$$\rho = \frac{4}{\sqrt{3}}\frac{1}{a^2 N} \tag{6}$$

$$\Delta G^{\gamma\to\varepsilon} = \sum x_i \Delta G_i^{\gamma\to\varepsilon} + \sum x_i x_j \Omega_{ij}^{\gamma\to\varepsilon} \tag{7}$$

where ρ is the molar surface density of the {111} plane, $\Delta G^{\gamma\to\varepsilon}$ is the Gibbs free-energy difference between the γ-austenite and the ε-martensite, $\sigma^{\gamma\to\varepsilon} = 7.5$ mJ/m^2 is the interface energy [45], a and N are lattice and Avogadro constants, respectively, $x_{i,j}$ is the molar fraction of the components, i and j, $\Delta G_i^{\gamma\to\varepsilon}$ is the Gibbs free-energy difference of γ and ε, $\Omega_{ij}^{\gamma\to\varepsilon}$ is the Gibbs free-energy difference of γ and ε of a binary system with components, i and j. All parameters are listed in Table 1. The stacking-fault energy of the current alloy is about 52.7 mJ/m^2. When the stacking-fault energy is greater than 40 mJ/m^2, the plastic deformation of fcc alloys is usually dominated by the dislocation slip [46], which is consistent with the microstructure characteristics of the quasi-static tensile samples. Apart from the stacking-fault energy, strain rate is another pivotal factor affecting the deformation modes of the alloy. Deformation twins are commonly found in alloys deformed at high strain rates. The reason why there are no twins in this alloy is that the critical twinning stress is significantly increased due to the tiny size of the matrix channel.

5. Conclusions

In the present work, a precipitation-hardening $Co_{40}Cr_{20}Ni_{30}Mo_2Al_4Ti_4$ HEA was developed, which presents excellent dynamic-mechanical properties. The deformation mechanisms of the alloy under quasi-static and dynamic tension were revealed. The conclusions are summarized as follows.

(1) A large number of coherent ordered $L1_2$ particles were observed in the current alloy. The diameter and volume fraction of $L1_2$ precipitates are about 7.8 nm and 9.85%, respectively.
(2) The current alloy possesses an excellent strength-plastic synergy in dynamic tension. When the strain rate is 1700/s, the yield and ultimate tensile strengths of the alloy are 950 MPa and 1725 MPa, respectively. In addition, it can still maintain a large elongation of 40%.
(3) In a quasi-static state, the plastic-deformation mode of the alloy is dislocation slip. During dynamic tension, stacking faults as an additional deformation mechanism promotes the high strength and effective work hardening of the alloy.
(4) The fine and dispersed $L1_2$ particles reduce the sizes of the matrix channel and twinning source, which greatly increases the critical twinning stress. Therefore, the formation of twins under dynamic tension is inhibited.

CRediT authorship contribution statement

J.L. Yuan: Conceptualization, Data curation, Writing – original draft. **Z.M. Jiao:** Resources, Data curation. **Z. Wang:** Resources, Data curation. **J.W. Qiao:** Writing – review & editing, Project administration. **P.D. Han:** Writing – review & editing. **Z.H. Wang:** Writing – review & editing, Project administration. **P.K. Liaw:** Writing – review & editing.

Declaration of competing interest

The authors declare that they have no known competing financial interests or personal relationships that could have appeared to influence

Table 1
Relevant parameters of stacking-fault energy.

Parameter	Thermodynamic function (J/mol)	Reference
$\Delta G_{Co}^{\gamma\to\varepsilon}$	−427.59 + 0.615T	[47]
$\Delta G_{Cr}^{\gamma\to\varepsilon}$	−2846-0.163T	[47]
$\Delta G_{Ni}^{\gamma\to\varepsilon}$	1046 + 1.255T	[47]
$\Delta G_{Al}^{\gamma\to\varepsilon}$	2800+5T	[47]
$\Delta G_{Ti}^{\gamma\to\varepsilon}$	−6000 + 0.1T	[47]
$\Delta G_{Mo}^{\gamma\to\varepsilon}$	−3650–0.63T	[47]
$\Omega_{CoCr}^{\gamma\to\varepsilon}$	−4621.59 + 7.32T+(7341.73–7.93T)(X_{Co}-X_{Cr})	[48]
$\Omega_{CoNi}^{\gamma\to\varepsilon}$	−820-1.65T	[49]
$\Omega_{CoAl}^{\gamma\to\varepsilon}$	27,956.3–13.9659T-28,740(X_{Al}-X_{Co})	[50]
$\Omega_{CoTi}^{\gamma\to\varepsilon}$	65,258-29.109T-16,240(X_{Co}-X_{Ti})	[51]
$\Omega_{CoMo}^{\gamma\to\varepsilon}$	241.4 + 12.8T+(-26,593.7–17.31T)(X_{Co}-X_{Mo})	[52]

the work reported in this paper.

Data availability

Data will be made available on request.

Acknowledgments

The authors would like to acknowledge the financial support of the National Natural Science Foundation of China (Nos. 52271110 and 12225207). PKL very much appreciates the supports from (1) the National Science Foundation (DMR-1611180, 1809640, and 2226508) and (2) the Army Research Office (W911NF-13-1-0438 and W911NF-19-2-0049).

Appendix A. Supplementary data

Supplementary data to this article can be found online at https://doi.org/10.1016/j.msea.2023.144727.

References

[1] J.W. Yeh, S.K. Chen, S.J. Lin, J.Y. Gan, T.S. Chin, T.T. Shun, C.H. Tsau, S.Y. Chang, Nanostructured high-entropy alloys with multiple principal elements: novel alloy design concepts and outcomes, Adv. Eng. Mater. 6 (5) (2004) 299–303.
[2] B. Cantor, I.T.H. Chang, P. Knight, A.J.B. Vincent, Microstructural development in equiatomic multicomponent alloys, Mater. Sci. Eng., A 375–377 (2004) 213–218.
[3] Y. Zhang, T.T. Zuo, Z. Tang, M.C. Gao, K.A. Dahmen, P.K. Liaw, Z.P. Lu, Microstructures and properties of high-entropy alloys, Prog. Mater. Sci. 61 (2014) 1–93.
[4] B. Gludovatz, A. Hohenwarter, D. Catoor, E.H. Chang, E.P. George, R.O. Ritchie, A fracture-resistant high-entropy alloy for cryogenic applications, Science 345 (6201) (2014) 1153–1158.
[5] J.P. Liu, X.X. Guo, Q.Y. Lin, Z.B. He, X.H. An, L.F. Li, P.K. Liaw, X.Z. Liao, L.P. Yu, J.P. Lin, L. Xie, J.L. Ren, Y. Zhang, Excellent ductility and serration feature of metastable CoCrFeNi high-entropy alloy at extremely low temperatures, Sci. China Mater. 62 (6) (2019) 853–863.
[6] T. Yang, Y.L. Zhao, W.H. Liu, J.J. Kai, C.T. Liu, $L1_2$-strengthened high-entropy alloys for advanced structural applications, J. Mater. Res. 33 (19) (2018) 2983–2997.
[7] T. Yang, Y.L. Zhao, Y. Tong, Z.B. Jiao, J. Wei, J.X. Cai, X.D. Han, D. Chen, A. Hu, J. J. Kai, K. Lu, Y. Liu, C.T. Liu, Multicomponent intermetallic nanoparticles and superb mechanical behaviors of complex alloys, Science 362 (6417) (2018) 933–937.
[8] Y. Tong, D. Chen, B. Han, J. Wang, R. Feng, T. Yang, C. Zhao, Y.L. Zhao, W. Guo, Y. Shimizu, C.T. Liu, P.K. Liaw, K. Inoue, Y. Nagai, A. Hu, J.J. Kai, Outstanding tensile properties of a precipitation-strengthened $FeCoNiCrTi_{0.2}$ high-entropy alloy at room and cryogenic temperatures, Acta Mater. 165 (2019) 228–240.
[9] T. Yang, Y.L. Zhao, J.H. Luan, B. Han, J. Wei, J.J. Kai, C.T. Liu, Nanoparticles-strengthened high-entropy alloys for cryogenic applications showing an exceptional strength-ductility synergy, Scripta Mater. 164 (2019) 30–35.
[10] P. Pandey, S. Kashyap, D. Palanisamy, A. Sharma, K. Chattopadhyay, On the high temperature coarsening kinetics of γ' precipitates in a high strength $Co_{37.6}Ni_{35.4}Al_{9.9}Mo_{4.9}Cr_{5.9}Ta_{2.8}Ti_{3.5}$ fcc-based high entropy alloy, Acta Mater. 177 (2019) 82–95.
[11] J. Moon, S.I. Hong, J.B. Seol, J.W. Bae, J.M. Park, H.S. Kim, Strain-rate sensitivity of high-entropy alloys and its significance in deformation, Mater. Res. Lett. 7 (12) (2019) 503–509.
[12] J. Moon, S.I. Hong, J.W. Bae, M.J. Jang, D. Yim, H.S. Kim, On the strain rate-dependent deformation mechanism of CoCrFeMnNi high-entropy alloy at liquid nitrogen temperature, Mater. Res. Lett. 5 (7) (2017) 472–477.
[13] Z.G. Wu, Y.F. Gao, H.B. Bei, Thermal activation mechanisms and Labusch-type strengthening analysis for a family of high-entropy and equiatomic solid-solution alloys, Acta Mater. 120 (2016) 108–119.
[14] M. Komarasamy, N. Kumar, R.S. Mishra, P.K. Liaw, Anomalies in the deformation mechanism and kinetics of coarse-grained high entropy alloy, Mater. Sci. Eng., A 654 (2016) 256–263.
[15] S. Basu, Z.M. Li, K.G. Pradeep, D. Raabe, Strain rate sensitivity of a TRIP-assisted dual-phase high-entropy alloy, Front. Mater. 5 (2018) 30.
[16] Q. Wei, Strain rate effects in the ultrafine grain and nanocrystalline regimes—influence on some constitutive responses, J. Mater. Sci. 42 (2007) 1709–1727.
[17] S.N. Nasser, W.G. Guo, Thermomechanical response of DH-36 structural steel over a wide range of strain rates and temperatures, Mech. Mater. 35 (11) (2003) 1023–1047.
[18] K.M. Cho, S.H. Lee, S.R. Nutt, J. Duffy, Adiabatic shear band formation during dynamic torsional deformation of an HY-100 steel, Acta Mater. 41 (1993) 923–932.
[19] J.M. Park, J. Moon, J.W. Bae, M.J. Jang, J. Park, S. Lee, H.S. Kim, Strain rate effects of dynamic compressive deformation on mechanical properties and microstructure of CoCrFeMnNi HEA, Mater. Sci. Eng., A 719 (2018) 155–163.
[20] J.Y. He, Q. Wang, H.S. Zhang, L.H. Dai, T. Mukai, Y. Wu, X.J. Liu, H. Wang, T. G. Nieh, Z.P. Lu, Dynamic deformation behavior of a face-centered cubic FeCoNiCrMn HEA, Sci. Bull. 63 (2018) 362–368.
[21] K. Jiang, T.F. Ren, G.B. Shan, T. Ye, L.Y. Chen, C.X. Wang, F. Zhao, J.G. Li, T. Suo, Dynamic mechanical responses of the $Al_{0.1}$CoCrFeNi high entropy alloy at cryogenic temperature, Mater. Sci. Eng., A 797 (2020), 140125.
[22] Z. Li, S. Zhao, H. Diao, P.K. Liaw, M.A. Meyers, High-velocity deformation of $Al_{0.3}$CoCrFeNi high-entropy alloy: remarkable resistance to shear failure, Sci. Rep. 7 (1) (2017), 42742.
[23] S. Gangireddy, K.M. Liu, B. Gwalani, R. Mishra, Microstructural dependence of strain rate sensitivity in thermomechanically processed $Al_{0.1}$CoCrFeNi high entropy alloy, Mater. Sci. Eng., A 727 (2018) 148–159.
[24] S. Gangireddy, B. Gwalani, R.S. Mishra, Grain size dependence of strain rate sensitivity in a single phase FCC high entropy alloy $Al_{0.3}$CoCrFeNi, Mater. Sci. Eng., A 736 (2018) 344–348.
[25] C.M. Cao, W. Tong, S.H. Bukhari, J. Xu, Y.X. Hao, P. Gu, H. Hao, L.M. Peng, Dynamic tensile deformation and microstructural evolution of Al_xCrMnFeCoNi high-entropy alloys, Mater. Sci. Eng., A 759 (2019) 648–654.
[26] P. Gao, Z.H. Ma, J. Gu, S. Ni, T. Suo, Y.L. Li, M. Song, Y.W. Mai, X.Z. Liao, Exceptional high-strain-rate tensile mechanical properties in a CrCoNi medium-entropy alloy, Sci. China Mater. 65 (3) (2022) 811–819.
[27] T.W. Zhang, S.G. Ma, D. Zhao, Y.C. Wu, Y. Zhang, Z.H. Wang, J.W. Qiao, Simultaneous enhancement of strength and ductility in a NiCoCrFe high-entropy alloy upon dynamic tension: micromechanism and constitutive modeling, Int. J. Plast. 124 (2020) 226–246.
[28] L. Fan, T. Yang, Y.L. Zhao, J.H. Luan, G. Zhou, H. Wang, Z.B. Jiao, C.T. Liu, Ultrahigh strength and ductility in newly developed materials with coherent nanolamellar architectures, Nat. Commun. 11 (1) (2020) 6240.
[29] S. Chen, H.S. Oh, B. Gludovatz, S.J. Kim, E.S. Park, Z. Zhang, R.O. Ritchie, Q. Yu, Real-time observations of TRIP-induced ultrahigh strain hardening in a dual-phase CrMnFeCoNi high-entropy alloy, Nat. Commun. 11 (2020) 826.
[30] Y.Y. Zhao, H.W. Chen, Z.P. Lu, T.G. Nieh, Thermal stability and coarsening of coherent particles in a precipitation-hardened $(NiCoFeCr)_{94}Ti_2Al_4$ high-entropy alloy, Acta Mater. 147 (2018) 184–194.
[31] A.J. Ardell, Precipitation hardening, Prog. Mater. Sci. 16 (12) (1985) 2131–2165.
[32] G.I. Taylor, The mechanism of plastic deformation of crystals. Part I.—Theoretical, Proc. R. Soc. A-Math. Phys. Eng. Sci. 145 (855) (1934) 362–387.
[33] Z. Wu, H. Bei, G.M. Pharr, E.P. George, Temperature dependence of the mechanical properties of equiatomic solid solution alloys with face-centered cubic crystal structures, Acta Mater. 81 (2014) 428–441.
[34] T.M. Pollock, A.S. Argon, Creep resistance of CMSX-3 nickel base superalloy single crystals, Acta Mater. 40 (1) (1992) 1–30.
[35] R.W. Kozar, A. Suzuki, W.W. Milligan, J.J. Schirra, M.F. Savage, T.M. Pollock, Strengthening mechanisms in polycrystalline multimodal nickel-base superalloys, Metall. Mater. Trans. A 40 (7) (2009) 1588–1603.
[36] D.S. Yan, Z. Yun, J.J. Li, Twin boundary spacing and loading direction dependent tensile deformation of nano-twinned $Al_{10}(CrCoFeNi)_{90}$ high-entropy alloy: an atomic study, Int. J. Mech. Sci. 242 (2023), 108026.
[37] Z.B. Zheng, H.K. Yang, A.P. Shatrava, J. Long, Y.H. Wang, J.X. Li, K.H. Zheng, Work hardening behavior and fracture mechanisms of Fe-18Mn-1.3C-2Cr low-density steel castings with varying proportions of aluminum alloying, Mater. Sci. Eng., A 862 (2023), 144467.
[38] M. Naeem, H.Y. He, F. Zhang, H.L. Huang, S. Harjo, T. Kawasaki, B. Wang, S. Lan, Z.D. Wu, F. Wang, Y. Wu, Z.P. Lu, Z.W. Zhang, C.T. Liu, X.L. Wang, Cooperative deformation in high-entropy alloys at ultralow temperatures, Sci. Adv. 6 (13) (2020), eaax4002.
[39] M. Yaghoobi, G.Z. Voyiadjis, The effects of temperature and strain rate in fcc and bcc metals during extreme deformation rates, Acta Mater. 151 (2018) 1–10.
[40] A. Hunter, D.L. Preston, Analytic model of the remobilization of pinned glide dislocations from quasi-static to high strain rates, Int. J. Plast. 70 (2015) 1–29.
[41] J.C. Cheng, H.L. Qin, C. Li, F. Zhao, R.C. Pan, Q.Y. Wang, Y.L. Bian, S.N. Luo, Deformation and damage of equiatomic CoCrFeNi high-entropy alloy under plate impact loading, Mater. Sci. Eng., A 862 (2023), 144432.
[42] K.P.D. Lagerlöf, J. Castaing, P. Pirouz, A.H. Heuer, Nucleation and growth of deformation twins: a perspective based on the double-cross-slip mechanism of deformation twinning, Philos. Mag. A 82 (15) (2002) 2841–2854.
[43] S. Yoshida, T. Bhattacharjee, Y. Bai, N. Tsuji, Friction stress and Hall-Petch relationship in CoCrNi equi-atomic medium entropy alloy processed by severe plastic deformation and subsequent annealing, Scripta Mater. 134 (2017) 33–36.
[44] S. Allain, J.P. Chateau, O. Bouaziz, S. Migot, N. Guelton, Correlations between the calculated stacking fault energy and the plasticity mechanisms in Fe-Mn-C alloys, Mater. Sci. Eng., A 387–389 (2004) 158–162.
[45] X.D. Yang, C.W. Li, M. Zhang, Z.H. Ye, X.Y. Zhang, M.Y. Zheng, J.F. Gu, H.H. Zhu, F. Wang, Study on tensile and thermal fatigue behaviors of additively manufactured cobalt-based alloys alloying with Al and Ni, Mater. Sci. Eng., A 840 (2022), 142914.
[46] Z.F. He, N. Jia, H.W. Wang, Y. Liu, D.Y. Li, Y.F. Shen, The effect of strain rate on mechanical properties and microstructure of a metastable FeMnCoCr high entropy alloy, Mater. Sci. Eng., A 776 (2020), 138982.
[47] A.T. Dinsdale, SGTE data for pure elements, Calphad 15 (1991) 317–425.
[48] K. Oikawa, G.W. Qin, T. Ikeshoji, R. Kainuma, K. Ishida, Direct evidence of magnetically induced phase separation in the fcc phase and thermodynamic

calculations of phase equilibria of the Co-Cr system, Acta Mater. 50 (9) (2002) 2223–2232.
[49] S.Y. Yang, M. Jiang, H.X. Li, Y. Liu, L. Wang, Assessment of Co-Cr-Ni ternary system by CALPHAD technique, Rare Met. 31 (2012) 75–80, 01.
[50] P.S. Wang, W. Xiong, U.R. Kattner, C.E. Campbell, E.A. Lass, O.Y. Kontsevoi, G. B. Olson, Thermodynamic re-assessment of the Al-Co-W system, Calphad 59 (2017) 112–130.
[51] N. Mattern, M. Zinkevich, J.H. Han, W. Löser, Experimental and thermodynamic assessment of the Co-Gd-Ti system, Calphad 54 (2016) 144–157.
[52] A. Davydov, U.R. Kattner, Thermodynamic assessment of the Co-Mo system, J. Phase Equil. 20 (1999) 5–16.